Chinese Chemical Letters 35 (2024) 109171

Contents lists available at ScienceDirect

Chinese Chemical Letters

journal homepage: www.elsevier.com/locate/cclet

O_2-generating multifunctional polymeric micelles for highly efficient and selective photodynamic-photothermal therapy in melanoma

Yu Qin[a,1], Mingyang Huang[a,1], Chenlu Huang[a], Hannah L. Perry[b], Linhua Zhang[a,*], Dunwan Zhu[a,*]

[a] Tianjin Key Laboratory of Biomedical Materials, Key Laboratory of Biomaterials and Nanotechnology for Cancer Immunotherapy, Institute of Biomedical Engineering, Chinese Academy of Medical Sciences & Peking Union Medical College, Tianjin 300192, China
[b] Molecular Sciences Research Hub, Department of Chemistry, White City Campus, Imperial College London, London W12 0BZ, United Kingdom

ARTICLE INFO

Article history:
Received 12 July 2023
Revised 26 September 2023
Accepted 5 October 2023
Available online 7 October 2023

Keywords:
Photodynamic therapy
Photothermal therapy
Oxygen generating
One-step self-assembly
Stimuli-responsive nanoparticles

ABSTRACT

Photothermal therapy (PTT) and photodynamic therapy (PDT) have received tremendous attention owing to their great potential for tumor treatment. However, two main issues hamper the antitumor performance of PDT: overexpression of glutathione (GSH) in tumors, which consumes PDT-induced reactive oxygen species (ROS), and hypoxia within the tumor microenvironment. The drawbacks of PTT include uneven temperature distribution and the upregulation of the heat-shock proteins in tumors, both of which result in ineffective treatment. To address these issues, a MnO_2 doped nano-delivery system (HTIM-PMs) was synthesized by one-step self-assembly of disulfide bond bridged copolymers for indocyanine green (ICG) and MnO_2 loading. The surface of polymeric micelles was layered with hyaluronan (HA) and transactivator (TAT) peptides to improve active targeting and increase cell penetration. After internalization, HTIM-PMs showed responsiveness to the tumor microenvironment (acid pH, high glutathione, high H_2O_2). Breaking the disulfide bond reduced the intratumoral GSH level and simultaneously released the MnO_2 and ICG. The released MnO_2 further reduced the GSH level and promoted O_2 generation, thus enhancing the PDT effect. The PTT-mediated hyperthermia accelerated blood flow, which is beneficial for O_2 distribution, and promotes ROS diffusion. These PTT-mediated adjuvant effects further overcame the limitations of PDT and the robust PDT effect in turn compensated for the deficiency of PTT. This promising platform exhibited a significant improvement in the PTT-PDT cancer treatment strategy compared to previously reported nanostructures.

Facing the challenge of the continuing cancer crisis, the development of an affordable and highly effective treatment with negligible toxicity is therefore pressing. Novel therapeutic strategies such as sonodynamic therapy (SDT) [1], phototherapy [2,3], immunotherapy [4], and combinations of therapies have been of increasing interest. Photothermal therapy (PTT) utilizes photothermal agents to convert photoenergy into hyperthermia upon near-infrared (NIR) laser irradiation for thermal ablation of tumor cells. Tumor vessels are tortuous, irregular, and lack normal hierarchical organization [5]. These properties limit blood transportation, leading to impaired heat dissipation and improved heat accumulation, which make tumors more sensitive to hyperthermia than normal cells [6]. However, it has been demonstrated that heat-shock proteins (HSPs) are upregulated in response to increased temperature, leading to the impediment of PTT efficacy. Moreover, uneven heat distribution in tumors also curtails the PTT effect. Therefore, combining PTT with other therapeutic strategies is a promising approach to maximizing efficacy and minimizing the side effects [7,8].

Photodynamic therapy (PDT) is a minimally invasive therapy that utilizes a photosensitizer activated by specific NIR light, inducing cell apoptosis through the generation of reactive oxygen species (ROS). PDT has proven to be an effective treatment option for esophageal, skin, and non-small cell lung cancers [9]. Many organic photosensitizers, such as indocyanine green [10], porphyrins, and chlorins [11], have been reported for clinical PDT. One of the mechanisms of PDT is that these photosensitizers convert intracellular oxygen into ROS under laser exposure, thus inducing tumor cell apoptosis. This process is dependent on O_2 supply which is contradicted by the fact that hypoxia occurs in malignant tumors. Therefore, alleviating the hypoxic conditions in tumor mi-

* Corresponding authors.
E-mail addresses: zhanglinhua@bme.pumc.edu.cn (L. Zhang), zhudunwan@bme.pumc.edu.cn (D. Zhu).
[1] These authors contributed equally to this work.

https://doi.org/10.1016/j.cclet.2023.109171
1001-8417/

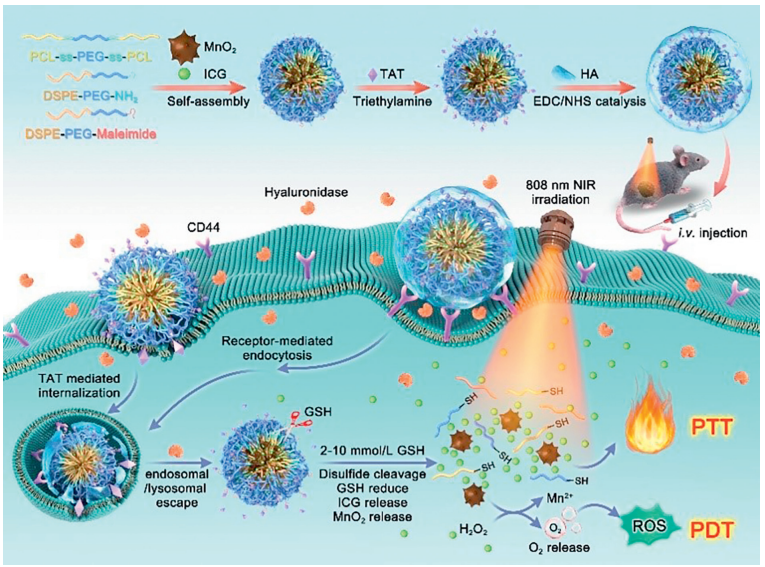

Scheme 1. Diagrammatic representation of the synthetic procedure and therapeutic mechanism of HTIM-PMs.

croenvironments is crucial for enhancing the effectiveness of PDT [12]. To overcome this challenge, various oxygen self-supplying agents, such as hemoglobin, perfluorocarbon liquid, catalase, and hydrogen peroxide catalysts, have emerged in recent years [13]. Among these, manganese dioxide (MnO_2) has been widely studied as an O_2 generating material because of its excellent catalytic performance in the decomposition of H_2O_2 [14–16]. The inadequate blood supply in tumors results in an elevated concentration of H_2O_2 (ranging between approximately 5×10^{-5} and 5×10^{-4} mol/L), surpassing levels found in normal physiological conditions (from analysis of literature and kinetics, the most likely range for plasma H_2O_2 is $1–5 \times 10^{-6}$ mol/L in human serum) [17–19]. In the presence of H_2O_2 and acidic conditions, MnO_2 is rapidly reduced to oxygen and Mn^{2+}, exerting a good performance for O_2 production in the hypoxic tumor.

For this work, a series of reduction-cleavable polymeric micelles (PMs) assembled from amphiphilic poly(ε-caprolactone)-ss-poly(ethylene glycol)-ss-poly(ε-caprolactone) (PCL-ss-PEG-ss-PCL) were chosen as the nano-delivery system for delivering MnO_2 and indocyanine green (ICG) due to their tumor-targeting ability, drug release properties, one-step surface functionalization and good biosafety [20,21]. Moreover, the dissociation of the disulfide bonds reduces glutathione (GSH) level in tumor and in turn decreases the off-target consumption of ROS. Transactivator (TAT), a cationic membrane penetrating peptide, has excellent transmembrane properties which has been utilized to enable nanomaterials to easily cross biofilm barriers and nuclear membranes [22,23]. However, the non-specific nature and rapid metabolic clearance of TAT leads to ineffective uptake, limiting its application [24]. To decrease the off-target membrane-penetrating activity of TAT, hyaluronan (HA) can be conjugated on nanoparticles, which can specifically target cancer cells that overexpress CD44, reducing off-target effects on healthy cells.

To optimize the therapeutic efficiency of combined PTT and PDT, in this study, O_2 generating multifunctional polymeric micelles (HTIM-PMs) were constructed. The pegylated hyaluronan shell was formed on the exterior surface to prevent the off-targeting effect of TAT and reduce systemic clearance. As illustrated in Scheme 1, when the HTIM-PMs were in proximity to the tumor, binding occurred through the interaction of the HA ligand and CD44 receptor. The TAT was then exposed after HA degradation, thus achieving active targeting and efficient membrane penetration of the tumor. The reducing microenvironment within the tumor consequently resulted in the disintegration of the HTIM-PMs, releasing MnO_2 and ICG. The high concentration of ICG facilitated the conversion of photoenergy to hyperthermia and the generation of ROS to promote tumor cell death. Furthermore, the presence of MnO_2 catalyzed the decomposition of endogenous hydrogen peroxide, increasing the supply of oxygen for ROS production and hence overcoming the main limitation of PDT treatment. Furthermore, the PTT-induced hyperthermia may have further accelerated the catalytic decomposition reaction and increased ROS diffusion, synergizing the anti-tumor effect of the PDT. By integrating multiple functions within the HTIM-PMs, higher efficiency of NIR-triggered ROS generation and photo-to-thermal conversion were achieved, which exemplified the benefits of combining PTT and PDT in cancer treatment.

The synthesis of MnO_2 particles was modified from Gao's work [25]. Briefly, 100 mg $KMnO_4$ was dissolved in deionized water. Then, 1.0 mL of oleic acid was introduced. The mixture was stirred for 5 h, after which crude brown-black particles were collected. The precipitate was dried at 60 °C and further treated by calcination at 350 °C in a furnace for 4 h to obtain purified MnO_2 with a smaller diameter size [26]. The MnO_2 particles and ICG-loaded polymeric micelles (IM-PMs) were subsequently synthesized through a thin-film hydration and sonication method. To bind HA and TAT to the surface of the PMs, 1,2-distearoyl-*sn*–glycero-3-phosphoethanolamine-*N*-[amino(polyethylene glycol)–2000] (DSPE-PEG(2000)-NH_2) and 1,2-distearoyl-*sn*–glycero-3-phosphoethanolamine-*N*-[maleimide(polyethylene glycol)–2000] (DSPE-PEG(2000)-Mal) were introduced into the mixture to generate a thin film. After the formation of a -maleimide and -NH_2 functionalized IM-PM dispersion, 0.4 mg TAT and 2 μL triethylamine were introduced at ambient temperature and stirred for 10 h to afford aminated TAT-IM-PMs. The shielding of the TAT began with the coupling of HA to aminated TAT-IM-PMs by EDC/NHS, according to a previously published method [25]. The HTIM-PMs were then separated from free agents by dialysis (dialysis bag MWCO 300 kDa) against 0.01 mol/L phosphate buffer saline (PBS) overnight.

In order to investigate the physical properties of the samples, several analytical techniques were employed, including X-ray photoelectron spectroscopy (XPS), transmission electron microscopy (TEM), atomic force microscopy (AFM), and dynamic light scat-

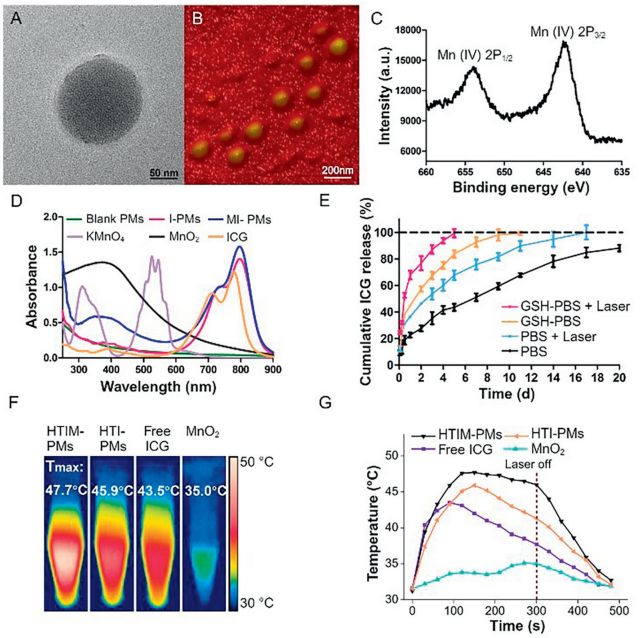

Fig. 1. *In vitro* morphology, drug releasing, and photothermal properties of the polymeric micelles. (A) TEM and (B) AFM images of the HTIM-PMs. Scale bar: 50 nm, 200 nm. (C) XPS spectrum of MnO_2. (D) Ultraviolet–visible spectroscopy (UV–vis) absorption spectra of blank PMs, I-PMs, MI-PMs, free ICG, MnO_2, and $KMnO_4$. (E) Releasing profiles of ICG from HTIM-PMs under various conditions ($n = 3$, each data point represents the mean ± standard deviation (SD) from three different readings). (F) Infrared thermal imaging and (G) Heating curves of the HTIM-PMs (500 μL, 15 μg/mL ICG), HTI-PMs (500 μL, 15 μg/mL ICG), free ICG (500 μL, 15 μg/mL ICG) and MnO_2 (500 μL, 4 μg/mL) under an 808 nm laser (1 W/cm^2) irradiation for 5 min.

Table 1
Diameter, zeta potential, size distribution, and drug loading of the PMs (mean ± SD, $n = 3$).

Sample	Diameter (nm)	PDI	Zeta potential (mV)	DL of ICG (%)	EE of ICG (%)
Blank PMs	100.83 ± 0.40	0.119	−12.90 ± 0.69	–	–
I-PMs	107.93 ± 0.42	0.179	−16.27 ± 0.38	8.64	94.52
TI-PMs	111.70 ± 0.17	0.184	−11.67 ± 0.42	–	–
HTI-PMs	134.77 ± 0.46	0.254	−12.53 ± 0.16	8.07	87.75
HTIM-PMs	158.70 ± 0.47	0.195	−14.43 ± 0.21	7.00	75.30

tering (DLS). The instruments used for these measurements are detailed in the supporting information. Successful modification of the polymeric micelles with HA was confirmed by TEM (Fig. 1A) which showed that the HTIM-PMs was spherical in shape with a 158.70 ± 0.47 nm diameter and a uniformly dense HA layer surrounding the entire surface. The TEM image (Fig. S1 in Supporting information) showed the size of the MnO_2 particles is around 8 nm, confirming the suitability of MnO_2 for encapsulation purposes. The spherical structure and narrow size distribution of the HTIM-PMs were also verified by AFM (Fig. 1B). Size, morphology, and surface chemistry play a pivotal role in affecting a nanomaterial's circulation time and hence the treatment's corresponding performance. In this research, the size of the various PMs ranged from ~100 nm to 160 nm, which makes them suitable for intravenous injection. As recorded in Table 1, the diameter of the HTIM-PMs (loaded with MnO_2 and ICG, 158.70 ± 0.47 nm) was larger than that of the HA targeted and TAT functionalized polymeric micelles encapsulated with MnO_2 particles and ICG (HTI-PMs, 134.77 ± 0.46 nm, loaded ICG alone). The drug loading of the HTIM-PMs (7.00%) was decreased compared to the HTI-PMs (8.07%). Both of these observations indicated that MnO_2 was encapsulated into the inner lumen of the HTIM-PMs.

To decorate HA and TAT on the surface of the PMs, DSPE-PEG-Mal, and DSPE-PEG-NH_2 were introduced during the preparation process. DSPE is highly hydrophobic and therefore preferentially incorporated into the PCL core of the PMs, occupying the entire volume of the hydrophobic inner cavity of the PMs. As shown in Table 1, this phenomenon resulted in higher drug loading (8.64%) and encapsulation efficiency of the ICG-loaded PMs (I-PMs, 94.52%) than the HTI-PMs (8.07% and 87.75% drug loading and encapsulation efficiency, respectively). The hydrophilic PEG-Mal and PEG-NH_2 chains on the surface of the micelles are linked with the TAT peptide and the targeting unit (HA) through covalent bonds. TAT is comprised of short amino acid groups, which confers the cationic property of TAT [27]. Zeta potential (Table 1) showed that the electronegativity of the TAT functionalized and ICG loaded polymeric micelles (TI-PMs, −11.67 ± 0.42 mV) decreased when TAT was modified on the surface of the I-PMs (−16.27 ± 0.38 mV), indicating that the addition of TAT to the surface of PMs was successful. With the introduction of HA through the PEG-NH_2 chains and electrostatic adsorption, the size of the HTI-PMs (134.77 ± 0.46 nm) increased compared to that of the TI-PMs (111.70 ± 0.17 nm), and the potential decreased from −11.67 ± 0.42 mV (TI-PMs) to −12.53 ± 0.16 mV (HTI-PMs). Notably, the polydispersity indexes of all the PMs were less than 0.260, indicating a narrow particle size distribution.

The UV absorption spectra and XPS was performed as described in the Supporting information. As shown in Fig. 1C, two classical binding-energy peaks were observed at 653.82 and 642.22 eV, which corresponds to Mn $2p_{1/2}$ and Mn $2p_{3/2}$ [28], indicating the generation of MnO_2. After the reaction with oleic acid, the peaks of $KMnO_4$ (314, 528, and 550 nm) vanished, and a broad peak emerged at 300–450 nm (Fig. 1D), further confirming the formation of MnO_2. In Fig. 1D, a broad absorption peak on the spectrum for the MI-PMs is present in the same position as the peak seen for MnO_2, indicating the successful encapsulation of MnO_2. The ICG absorption peaks in the MI-PMs and I-PMs' spectrums were slightly red-shifted compared with the free ICG, which was most likely caused by the interaction between the ICG and the PMs.

The *in vitro* drug release pattern of the HTIM-PMs under different conditions was studied. As shown in Fig. 1E, 22.65% of ICG was released from the PMs into PBS after 24 h, while with laser irradiation, the cumulative ICG release reached 36.56% and in the group of GSH-PBS + laser (with the aid of laser irradiation and GSH stimulation), the cumulative ICG release significantly increased to 67.83%. Furthermore, more than 90% of ICG was released from the HTIM-PMs in the group of GSH-PBS + laser after 4 days, while in the PBS group (simulated normal physiological conditions), the HTIM-PMs displayed sustained release properties with 88.13% of ICG being released after 20 days. These results demonstrate the stimuli responsiveness of the HTIM-PMs and the consequently excellent controlled release ability of this delivery system under external and internal environment stimuli.

As displayed in Figs. 1F and G, the thermometer reading of the HTIM-PMs and HTI-PMs was significantly higher than that of free ICG after laser irradiation, most likely owing to the slow heat dissipation of the PMs. Interestingly, it was found that the maximum temperature of the MnO_2 group rose to 35.0 °C after laser irradiation, which revealed that MnO_2 also exhibits photo-thermal conversion ability. Meanwhile, the temperature rise of the HTIM-PMs (maximum temperature 47.7 °C) was higher than that of the HTI-PMs, again confirming that MnO_2 contributes to the photo-thermal conversion.

In an acidic environment with H_2O_2, MnO_2 is rapidly reduced to O_2 and Mn^{2+}, relieving the hypoxic environment in tumor cells, and improving the effectiveness of PDT. The O_2 and intracellular ROS generation were detected using the $[Ru(dpp)_3]Cl_2$(RDPP) probe and carboxy-H_2DCFDA separately according to the instructions. The detailed procedures can be found in the supporting information.

In vitro studies revealed that the number of oxygen bubbles generated by the reaction of HTIM-PMs and H_2O_2 increased with increasing H_2O_2 concentration. Obvious bubbles were produced at an H_2O_2 concentration of 1×10^{-4} mol/L (close to the H_2O_2 concentration found in the tumor microenvironment; Fig. S2A in Supporting information). Oxygen generation was further detected by the RDPP probe. The RDPP consumption curves revealed that the HTIM-PMs were able to promote O_2 generation under acidic environment (pH 5.5) and H_2O_2 conditions. By contrast, no significant RDPP fluorescence decay was observed in the HTI-PMs group, demonstrating that MnO_2 plays a role in oxygen generation (Fig. S2B in Supporting information). 1,3-Diphenylisobenzofuran (DPBF) is a fluorescent probe that can be irreversibly oxidized by ROS. Therefore, DPBF was used to semi-quantify the ROS production of the HTIM-PMs at different concentrations of H_2O_2 with or without laser irradiation. As shown in Fig. S2C (Supporting information), the absorbance of DPBF in the HTIM-PMs suspension gradually declined after laser irradiation, and the rate of fluorescence decay accelerated with the increase of H_2O_2 concentration. These results confirmed that the HTIM-PMs were able to significantly increase the production of ROS in response to the addition of H_2O_2.

The same trend of *in vitro* O_2 and ROS generation was demonstrated at an intracellular level. The production of O_2 and ROS in B16-F10 melanoma cells were visualized by confocal laser scanning microscopy (CLSM), where the O_2 probe was RDPP and the ROS probe was carboxy-H_2DCFDA. The CLSM images of O_2 generation (Fig. S2D in Supporting information) showed that the RDPP fluorescence (orange fluorescence) attenuated rapidly with the increase of HTIM-PMs incubation time, which was not seen with the PBS group, indicating that the HTIM-PMs were catalyzing the production of O_2 from intracellular H_2O_2, thus alleviating hypoxia. As shown in Fig. S3 (Supporting information), robust carboxy-H_2DCFDA fluorescence in the cytoplasm of the HTIM-PMs + laser and HTI-PMs + laser treatment groups were detected, and the flow cytometry graph exhibited the fluorescence intensity of carboxy-H_2DCFDA in HTIM-PMs + laser group (44.6%) was stronger than that of the HTI-PMs + laser treated group (32.1%). In comparison, no significant carboxy-H_2DCFDA fluorescence was detected in the PBS, PBS + laser, HTI-PMs, or HTIM-PMs treated groups (flow cytometry analysis showed the fluorescence intensity in these groups was below 8%). The above results suggested that the encapsulation of MnO_2 nanoparticles can promote O_2 production and thereby enable enough O_2 to be converted into ROS under laser irradiation.

The polymeric micelles (carrier materials) were composed of PEG and PCL, which are FDA-approved materials due to their biodegradability and biocompatibility [29]. ICG is a clinically approved, near-infrared tricarbocyanine dye. HA is a well-studied glycosaminoglycan that exists naturally in the human body and is widely used in the biopharmaceutical and cosmetic industries [30,31]. MnO_2 serves as a catalytic agent for the decomposition reaction of H_2O_2 into O_2 and soluble Mn^{2+}, and Mn^{2+} is an essential metal ion that participates in many critical biological functions [32]. Therefore, the toxicity of the oxygen-generating PMs delivery system is theoretically negligible. Indeed, the results of the cytotoxicity study (Fig. S4A in Supporting information) suggested that the cytotoxicity of the HTIM-PMs, HTI-PMs, HTM-PMs, and free ICG was negligible at a range of concentrations. However, crucially for their use in PTT/PDT, with the aid of 808 nm laser irradiation, the percentage survival of B16-F10 cells dropped to less than 5% in the HTIM-PMs, HTI-PMs, and free ICG treated groups, when ICG concentration increased to 30 μg/mL. After laser treatment, the HTIM-PMs treated group showed the most potent cytotoxic effects, followed by the HTI-PMs at the equivalent ICG concentration of 15 μg/mL. By contrast, no obvious toxicity was noted in the HTM-PMs treated group due to the lack of ICG loading, preventing the HTM-PMs from responding to the laser irradiation. These results indicated that laser-induced PDT-PTT can be effective in killing tumor cells and that the efficacy of treatment is ICG concentration-dependent (Fig. S4B in Supporting information). For further validation of the laser-induced cytotoxic effect of the different PMs, a calcein-AM and propidium iodide (PI) kit was used post-treatment to stain for imaging the live and dead cells. As exhibited in Fig. S4C (Supporting information), substantial cell death occurred upon laser irradiation in the HTIM-PMs and HTI-PMs treated groups, while for the PBS group, no significant change was found before and after laser irradiation. This finding further confirmed the therapeutic effects that can be achieved when HTIM-PMs are administered with 808 nm laser exposure.

As shown in the confocal laser scanning microscopy images (Fig. 2), the red fluorescence of ICG could be detected in the cytoplasm of tumor cells in all the PMs treated groups, indicating that this multifunctional PMs delivery system exhibit efficient internalization by tumor cells. ICG fluorescence in the cytoplasm of the I-PMs treated group was weaker than that of HI-PMs (19.5% and 24.5% obtained from flow cytometry analysis, respectively), indicating that the HA-modified PMs were able to anchor to the over-

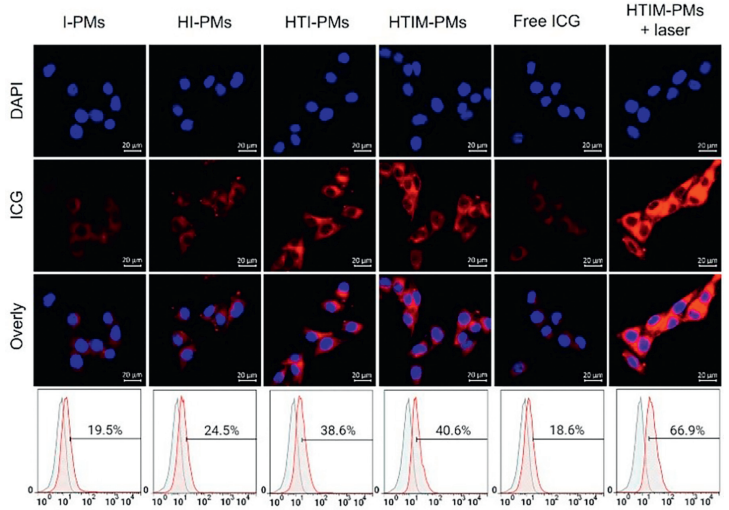

Fig. 2. Intracellular accumulation of ICG after cells were incubated with I-PMs, HI-PMs, HTI-PMs, HTIM-PMs, and free ICG. Cells were stained with 4′,6-diamidino-2-phenylindole (DAPI). Scale bar: 20 μm. The last line represents flow cytometric analysis of ICG in cells after treatments.

expressed CD44 receptor on the membrane of B16-F10 melanoma cells, enhancing cellular uptake of the drug through a receptor-ligand binding mechanism. After modification of the HI-PMs with TAT peptide, the intracytoplasmic ICG fluorescence was enhanced further (38.6% of fluorescence obtained from flow cytometry analysis), compared to the I-PMs and HI-PMs treated groups. This result demonstrated that the TAT peptide possesses superior transmembrane properties, thus improving the efficiency of drug internalization. The ICG fluorescence intensity of the HTIM-PMs group (40.6%) was close to that of the HTI-PMs (38.6%) group, indicating that the encapsulation of MnO_2 in the PMs delivery system does not affect the cellular uptake. The ICG fluorescence was significantly enhanced in the laser-irradiated HTIM-PMs group, suggesting that the laser-activated hyperthermia from ICG increased the fluidity of the cell membrane and thereby enhance cellular uptake. Moreover, laser-induced hyperthermia and ROS production are known to promote cell apoptosis, leading to cell membrane permeabilization, which is beneficial for effective cellular uptake.

In line with our previously reported *in vivo* drug distribution study [20], NIR irradiation (808 nm, 0.3 W/cm^2, 5 min) was administered 24 and 48 h after intravenous tail injection of the PMs. All experiments involving animals were strictly carried out following the guidelines approved by the Chinese Academy of Medical Science and Peking Union Medical College, and the detailed experimental procedure can be found in Supporting information. The thermal images (Fig. 3A) showed that the combination of HTIM-PMs plus laser irradiation afforded the greatest hyperthermia, reaching a maximum tumor temperature of 57.1 °C, which was high enough to achieve tumor ablation. A maximum temperature of 45.8 °C was recorded for the PBS group, however, this was due to the black color of the B16-F10 melanoma, which facilitated the absorption of light energy and the conversion of that energy into heat energy. Although it has been reported that cells suffer irreparable damage from hyperthermia at 42–48 °C through the folding and denaturation of proteins, a lasting effect is only observed in cases where these temperatures are maintained for at least one hour [6]. Therefore, the photothermal effect observed in the PBS group here was considered to be limited.

According to Figs. 3C–E, there was no significant difference in the tumor volume or weight between the PBS control group and the PBS + laser group at the end of treatment ($P < 0.05$), indicating that the laser treatment alone could not suppress tumor growth. This was due primarily to the high metastatic and invasive properties of malignant B16-F10 melanoma cells and the limited photothermal effect that can be achieved without the aid of a photothermal conversion agent [33]. For the free ICG group, the maximum temperature reached 46.9 °C (Fig. 3A) which was slightly higher than that of the PBS group, and the temperature elevation trend curve of the free ICG group closely aligns with that of the PBS group (Fig. 3B), suggesting that only a small amount of ICG accumulated within tumor. Although the maximum temperature of the free ICG + laser group exceeded the theoretical temperature required to cause irreversible cell damage, the observed effect on the suppression of tumor progression was weak. This was especially evident at the later stage of treatment when the growth of the tumor volume was very fast and seemingly uninhibited by the PTT. In sharp contrast, the maximum temperature of HTI-PMs + laser group reached 53.3 °C, which was great enough to effectively slow the rate of tumor growth. However, it is important to note that this treatment group was not able to completely eradicate the tumor cells, and the tumors did continue to grow, albeit at a reduced rate. The maximum temperature achieved by the IM-PMs + laser and HTIM-PMs + laser groups, was 53.9 and 57.1 °C, respectively, most likely due to the higher drug accumulation in these treatment groups. Most importantly, the HTIM-PMs + laser treatment group performed significantly better than the HTI-PMs + laser group and exerted outstanding antitumor effectiveness, demonstrating the value of considering hypoxia in the design of such photothermal agents. The hypoxic microenvironment is a common feature among various tumors, and B16-F10 is no exception [34]. The hypoxic environment is unfavorable for efficient photodynamic therapy as the lack of O_2 limits the generation of ROS. Hence, the outstanding achievement in the HTIM-PMs + laser group was the ability to relieve the hypoxia within the tumor, which resulted in an enhanced PDT effect. Collectively, these results demonstrated that both the IM-PMs + laser and HTIM-PMs + laser groups exhibited a synergistic PDT-PTT therapeutic effect and effectively ablated tumors *in vivo*. Furthermore, surface modification of the PMs with HA and TAT boosted the antitumor effect ($P < 0.05$) due to the increased accumulation of these PMs within the tumor tissue. The body weights of the tumor-bearing mice were measured throughout the investigation and although the weights increased slightly after treatment, no statistical difference between the treatment groups was found (Fig. 3F), demonstrating that the PMs had good biocompatibility.

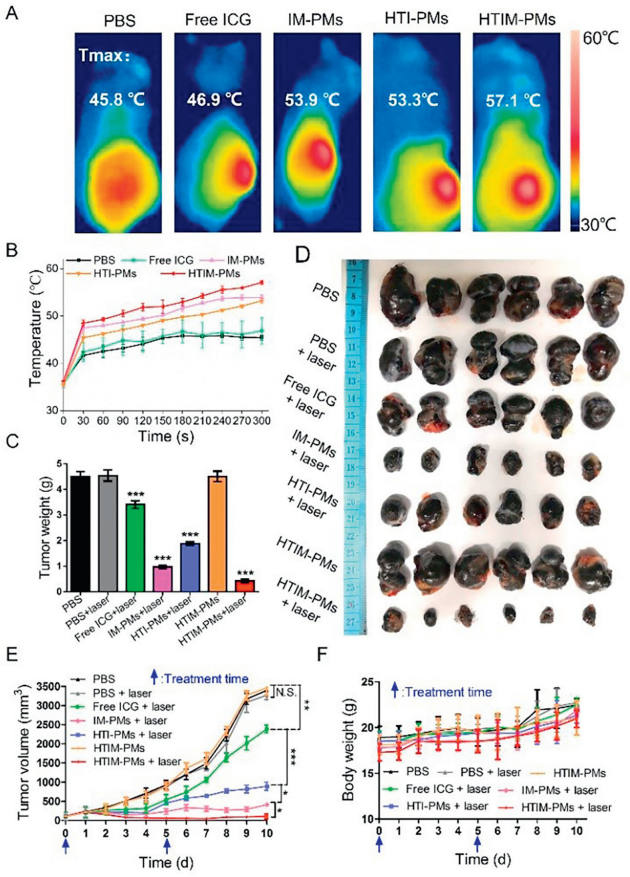

Fig. 3. Assessments of *in vivo* photothermal therapy. (A) Infrared thermal imaging and (B) temperature changes of tumor areas within 5 min of laser irradiation (808 nm, 0.3 W/cm^2) 24 h post drug administration. Each data point represents the mean ± SD from three different readings. (C) Weight and (D) images of tumors collected from tumor-bearing mice 10 days post-therapy. $^{***}P < 0.001$ *vs.* PBS control group. (E) Change in tumor volume and (F) body weight of tumor-bearing mice upon treatments ($n = 6$). $^{*}P < 0.05$, $^{**}P < 0.01$, $^{***}P < 0.001$. N.S. represents no significant difference between groups. Each data point represents the mean ± SD from six different readings.

Fluorescence imaging, immunofluorescence, the intracellular accumulation of ROS, and tumor apoptosis level were explored to explain how the multifunctional PMs ICG delivery system functions in tumor treatment. The detailed procedures can be found in the supporting information. After 24 h of treatment, all of the tumor

tissues were removed, and frozen sections were examined using fluorescence microscopy. According to the top row of Fig. S5 (Supporting information), red fluorescent signals were viewed in the tumor cells injected with HTI-PMs and HTIM-PMs, indicating that HA and TAT modified PMs can efficiently target to the tumor site and improve intratumoral ICG accumulation. The fluorescence intensity of ICG in IM-PMs treated group was weaker than that observed in the HTI-PMs and HTIM-PMs treated group, but significantly more intense than that observed in the free ICG treated group, confirming the passive targeting effect of the IM-PMs due to their appropriate particle size and morphology. The second row of hypoxia immunofluorescence staining shows that the tumor tissue of the PBS, free ICG, and HTI-PMs groups remained highly hypoxic, as indicated by the presence of green fluorescence. This fluorescence is quenched in the IM-PMs and HTIM-PMs treatment groups, highlighting the role of MnO_2 in the production of O_2 and the consequent relief of hypoxia. The intratumoral O_2 content directly affects the generation of ROS, which in turn affects therapeutic effect of PDT. Although the HTI-PMs group displayed a higher ICG intratumoral accumulation compared to the IM-PMs treated group, the ROS content in the HTI-PMs treated group was less than in the IM-PMs treated group. This is because the hypoxic environment within the tumor tissue of the HTI-PMs treated mice weakened the proficiency of ROS generation and thus attenuated the efficacy of PDT. In the HTIM-PMs group, a high concentration of ICG was detected in the tumor sections, which was supported by the presence of MnO_2, which catalyzed the decomposition of intratumoral H_2O_2 and afforded a high local concentration of O_2, which resulted in a large amount of ROS generation upon exposure to NIR laser irradiation and thus efficient cell apoptosis. In the group treated with just free ICG, the *in vivo* instability, fast elimination from the body, and the absence of specific targeting led to no detectable ICG accumulation within the tumor site. Furthermore, only a small amount of ROS was generated in the highly hypoxic environment and sporadic clusters of apoptotic cells were visualized using TUNEL staining. These results further corroborated the conclusion that (1) the HTIM-PMs are prone to accumulating at the tumor site due to the targeting ability and improved cell-penetrability; (2) the triggered O_2 release upon 808 nm NIR irradiation of the HTIM-PMs facilitated the generation of ROS and improved the PDT effect and (3) the HTIM-PMs provided a smart platform that facilitated a synergistic approach to treatment by combining both PDT and PTT agents in a single assembly, which resulted in robust destruction of tumor tissue.

In this study, we designed a novel PTT-PDT platform (HTIM-PMs) to treat high-invasive melanomas. The HTIM-PMs demonstrated efficient tumor accumulation resulting from the EPR effect, hyaluronic acid-guided targeting, and TAT-assisted cell penetration. Compared with traditional targeted tumor therapy, our HTIM-PMs benefit from high cell internalization efficiency and biocompatibility, due to the modification with hyaluronic acid shielded TAT peptide [35,36]. After internalization of the HTIM-PMs, the MnO_2 within the nano-delivery system was activated by the acidic and hypoxic tumor microenvironment, resulting in the decomposition of intratumoral H_2O_2 and relief in the intratumoral hypoxia, which led to an improvement in the efficacy in the PDT effect upon laser irradiation. The high intratumoral accumulation of ICG within the tumor afforded a high PTT effect upon laser irradiation and enhanced photo-to-thermal conversion was achieved with the assistance of MnO_2. Notably, it was shown that the hyperthermia generated by the HTIM-PMs succeeded in ablating the tumor cells and accelerating the degradation of H_2O_2 to further provide O_2 for an enhanced PDT effect. In conclusion, this oxygen-generating delivery system provided a promising platform for integrating PTT and PDT as a treatment for malignant tumors.

Declaration of competing interest

The authors declare that they have no known competing financial interests or personal relationships that could have appeared to influence the work reported in this paper.

Acknowledgments

We acknowledge financial support from the National Natural Science Foundation of China (Nos. 82172090 and 82072059), CAMS Innovation Fund for Medical Sciences (CIFMS, Nos. 2021-I2M-1–058 and 2022-I2M-1–023), Fundamental Research Funds for the Central Universities (No. 2019PT320028), Tianjin Municipal Natural Science Foundation (No. 20JCYBJC00030).

Supplementary materials

Supplementary material associated with this article can be found, in the online version, at doi:10.1016/j.cclet.2023.109171.

References

[1] X. Lin, J. Song, X. Chen, H. Yang, Angew. Chem. Int. Ed. 59 (2020) 14212–14233.
[2] X. Deng, Z. Shao, Y. Zhao, Adv. Sci. 8 (2021) 2002504.
[3] Z. Li, Y. Pan, S. Du, et al., Acta Pharm. Sin. B 12 (2022) 4224–4234.
[4] N. Wang, Y. Zuo, S. Wu, et al., Acta Pharm. Sin. B 12 (2022) 4486–4500.
[5] A.C. Dudley, Z.A. Khan, S.C. Shih, et al., Cancer Cell 14 (2008) 201–211.
[6] D. Jaque, L.M. Maestro, B. del Rosal, et al., Nanoscale 6 (2014) 9494–9530.
[7] S. Gou, N. Chen, X. Wu, et al., Acta Pharm. Sin. B 12 (2022) 406–423.
[8] X. Chen, X. Fan, Y. Zhang, et al., Acta Pharm. Sin. B 12 (2022) 3710–3725.
[9] D.E. Dolmans, D. Fukumura, R.K. Jain, Nat. Rev. Cancer 3 (2003) 380–387.
[10] H. Wu, C. Huang, L. Wang, et al., Chin. Chem. Lett. 33 (2022) 5035–5041.
[11] B. Zhang, L. Lin, J. Mao, et al., Chin. Chem. Lett. 34 (2023) 108518.
[12] X. Guo, J. Qu, C. Zhu, et al., Drug Deliv. 25 (2018) 585–599.
[13] Z. Zhou, J. Song, L. Nie, X. Chen, Chem. Soc. Rev. 45 (2016) 6597–6626.
[14] D. He, L. Hai, X. He, et al., Adv. Funct. Mater. 27 (2017) 1704089.
[15] M. Song, T. Liu, C. Shi, X. Zhang, X. Chen, ACS Nano 10 (2016) 633–647.
[16] Z. Ma, X. Jia, J. Bai, et al., Adv. Funct. Mater. 27 (2017) 1604258.
[17] W. Zhang, S. Li, X. Liu, et al., Adv. Funct. Mater. 28 (2018) 1706375.
[18] B. Halliwell, M.V. Clement, L.H. Long, FEBS Lett. 486 (2000) 10–13.
[19] H.J. Forman, A. Bernardo, K.J.A. Davies, Arch. Biochem. Biophys. 603 (2016) 48–53.
[20] L. Zhang, Y. Qin, Z. Zhang, et al., Acta Biomater. 75 (2018) 371–385.
[21] H. Wang, X. Yang, C. Hu, et al., Chin. Chem. Lett. 33 (2022) 4179–4184.
[22] N. Todorova, C. Chiappini, M. Mager, et al., Nano Lett. 14 (2014) 5229–5237.
[23] L. Pan, Q. He, J. Liu, et al., J. Am. Chem. Soc. 134 (2012) 5722–5725.
[24] M.M. Khan, N. Filipczak, V.P. Torchilin, J. Control. Release 330 (2021) 1220–1228.
[25] S. Gao, G. Wang, Z. Qin, et al., Biomaterials 112 (2017) 324–335.
[26] Z. Yang, Y. Zhang, W. Zhang, et al., J. Solid State Chem. 179 (2006) 679–684.
[27] S. Shan, S. Jia, T. Lawson, et al., Int. J. Mol. Sci. 20 (2019) 44–54.
[28] X. Jia, Y. Zhang, Y. Zou, et al., Adv. Mater. 30 (2018) e1704490.
[29] L. Zhang, Z. Chen, H. Wang, et al., RSC Adv. 6 (2016) 54727–54737.
[30] J. Wu, J. Zhang, C. Deng, et al., ACS Appl. Mater. Interfaces 9 (2017) 3985–3994.
[31] N.V. Rao, H.Y. Yoon, H.S. Han, et al., Expert Opin. Drug Deliv. 13 (2016) 239–252.
[32] A.P. Koretsky, A.C. Silva, NMR Biomed. 17 (2004) 527–531.
[33] X. Chen, S.A. Rotenberg, Cell Signal. 22 (2010) 1097–1103.
[34] J.M. Brown, W.R. Wilson, Nat. Rev. Cancer 4 (2004) 437–447.
[35] I. Gessner, I. Neundorf, Int. J. Mol. Sci. 21 (2020) 25–36.
[36] R. Jin, J. Xu, L. Duan, G. Gao, Carbohydr. Polym. 268 (2021) 118240.